Finite-field coupling via learning the charge response kernel

To cite this article: Yunqi Shao *et al* 2022 *Electron. Struct.* **4** 014012

Electronic Structure

OPEN ACCESS

RECEIVED
15 December 2021

REVISED
1 February 2022

ACCEPTED FOR PUBLICATION
1 March 2022

PUBLISHED
18 March 2022

PAPER

Finite-field coupling via learning the charge response kernel

Yunqi Shao[1], **Linnéa Andersson**[1], **Lisanne Knijff and Chao Zhang***

Department of Chemistry-Ångström Laboratory, Uppsala University, Lägerhyddsvägen 1, Box 538, 75121 Uppsala, Sweden
* Author to whom any correspondence should be addressed.
[1] These authors contributed equally to this work.

E-mail: chao.zhang@kemi.uu.se

Keywords: conceptual DFT, electronic polarization, machine learning, electrode–electrolyte interface, finite-field method, atomic charge

Supplementary material for this article is available online

Abstract

Response of the electronic density at the electrode–electrolyte interface to the external field (potential) is fundamental in electrochemistry. In density-functional theory, this is captured by the so-called charge response kernel (CRK). Projecting the CRK to its atom-condensed form is an essential step for obtaining the response charge of atoms. In this work, the atom-condensed CRK is learnt from the molecular polarizability using machine learning (ML) models and subsequently used for the response-charge prediction under an external field (potential). As the machine-learnt CRK shows a physical scaling of polarizability over the molecular size and does not (necessarily) require the matrix-inversion operation in practice, this opens up a viable and efficient route for introducing finite-field coupling in the atomistic simulation of electrochemical systems powered by ML models.

1. Introduction

Electrode–electrolyte interfaces involve a structural transition between an electronic conductor and an ionic conductor [1]. The dielectric mismatch between these two phases causes an intrinsic electric field at the interface [2]. Moreover, during the operation, an external bias will be applied and this leads to an additional electric field due to the electric double layer, which then modulates the reactivity at the electrochemical interface [3]. Therefore, capturing the electronic polarization and the charge transfer between the electrode and the electrolyte, as well as their responses to the external bias is crucial to the atomistic modelling of electrochemical interfaces.

Density functional theory based molecular dynamics (DFTMD) [4, 5], in principle, can provide a realistic representation of such interfaces where electronic, structural and dynamical properties are treated on an equal footing [6–11]. However, its power is limited in practice because of the accessible time and length scales, usually to hundreds of atoms and tens of picoseconds. Despite that there is recent progress on the development of implicit solvation models for modelling electrochemical interfaces [12–16], finite-temperature simulations and electrode dynamics are still out of reach. Therefore, a paradigm shift in multi-scale modelling of electrochemical interfaces is clearly needed.

The marriage of machine learning (ML) and DFTMD leads to recent advances in machine-learning potentials [17–20], which have begun to revolutionize the field of materials modelling [21]. Successful applications have been carried out for studying the morphology evolution of electrode materials [22, 23], the Green–Kubo conductivity of liquid electrolytes [24, 25] and the proton/water dynamics at oxide–water interfaces [26–28]. Nevertheless, the local descriptors used in these works depend only on the atom type and the atomic coordinates. The information of the electron density, needed for modelling the electrochemical interface, is not yet there in these popular representations [29].

As the proxy of electron density, environment-dependent atomic charge and dipole have been the target for ML predictions for both isolated molecules [30–34] and periodic systems [35, 36]. The same applies to the polarizability, where a number of ML models have emerged [37, 38]. Moreover, atomic charge, which contains

the non-local information, can be used as a descriptor for constructing ML potentials, as proposed recently [39, 40]. However, when it comes to the modelling of electrochemical systems, what is needed is not only a charge model depending on the local environment but also a response charge model sensitive to the external bias. Despite recent attempts to couple the molecular dipole to the external field [41, 42], the crucial link between charge and polarizability is missing in the current formulations of ML models.

This calls for the description of the response function [43], which has been seen as a cornerstone in conceptual DFT [44–48]. Earlier attempts before the establishment of conceptual DFT came under the umbrella of the so-called electronegativity equilibration method (EEM) [49, 50] and the charge equilibration method (QEq) [51]. Unfortunately, these charge models suffer from superlinear scaling of the polarizability for linear alkanes [52] and the incorrect dissociation limit [53], which stimulated a number of new developments to remedy these problems [54–57]. When it comes to the response charge, the chemical potential equalization (CPE) [58] and the atom-condensed Kohn–Sham DFT approximated to second order (ACKS2) [59] stand out due to a closer connection to conceptual DFT and a firmer foundation in the linear response theory. Nevertheless, the mathematical forms of bond hardness and atom hardness used in these methods are difficult to come by in practice, which motivates us to tackle this issue with the emerging ML technique for modelling molecules and materials, e.g. graph convolution neural network (GCNN) [60–62].

In this work, we first provide a unified view of CPE and ACKS2 using the charge response kernel (CRK), i.e. $\chi(\mathbf{r}, \mathbf{r}')$. This is achieved by exploring Dyson's equation and dielectric functions [63, 64], which are better known in the solid-state physics community. Further, this allows us to develop the GCNN framework PiNet-χ to learn the atom-condensed CRK by regressing molecular polarizability. The physical soundness of this procedure is tested by comparing the response charge and the machine-learning inferred atom-condensed CRK to the reference values. In particular, the PiNet-χ models show a physical scaling behaviour of the polarizability for both non-conjugated and conjugated systems, and does not (necessarily) require the matrix-inversion operation for generating the response charge. Thus, this provides a generic and efficient approach to introduce finite-field coupling in atomistic simulations powered by ML models.

In the following, we will first introduce the CRK, the reformulation of the CPE and ACKS2 methods in terms of the CRK and the advantages of using the CRK to describe molecular polarizability. Then, its machine-learning realizations with different flavours in the PiNet-χ framework are introduced. After introducing details of the dataset, model trainings and reference calculations, we show how different PiNet-χ models perform regarding molecular polarizability, size scaling as well as in examples of response charge and atom-condensed CRK. Finally, we conclude by providing a perspective on extending PiNet-χ for describing charge transfer in condensed phase and extended systems.

2. Theory and methods

2.1. Charge response kernel

In the density-functional theory (DFT) of atoms and molecules [45], the response function of charge density $\rho(\mathbf{r})$ to the external potential $\nu(\mathbf{r}')$ for a system of N_0 electrons is given by Berkowitz and Parr's classic work [65]:

$$\chi(\mathbf{r}, \mathbf{r}') = \left[\frac{\delta\rho(\mathbf{r})}{\delta\nu(\mathbf{r}')}\right]_{N_0} = -s(\mathbf{r}, \mathbf{r}') + \frac{s(\mathbf{r}')s(\mathbf{r})}{S}. \tag{1}$$

$\chi(\mathbf{r}, \mathbf{r}')$ is also called the CRK in the literature [66]. Apart from the obvious fact that $\chi(\mathbf{r}, \mathbf{r}') = \chi(\mathbf{r}', \mathbf{r})$, which means:

$$\boldsymbol{\chi} = \boldsymbol{\chi}^{\top}. \tag{2}$$

$\chi(\mathbf{r}, \mathbf{r}')$ satisfies the following sum rule $\int \chi(\mathbf{r}, \mathbf{r}')\mathrm{d}\mathbf{r}' = 0$, which can be rewritten in matrix form as:

$$1^{\top}\boldsymbol{\chi} = 0. \tag{3}$$

On the rhs of equation (1), $s(\mathbf{r}, \mathbf{r}')$ is the softness kernel, which is defined as:

$$s(\mathbf{r}, \mathbf{r}') = -\frac{\delta\rho(\mathbf{r})}{\delta u(\mathbf{r}')}, \tag{4}$$

where the modified potential $u(\mathbf{r}) = \nu(\mathbf{r}) - \mu$ and μ is the chemical potential of the system.

A related quantity, i.e. the hardness kernel $\eta(\mathbf{r}, \mathbf{r}')$, is defined as:

$$\eta(\mathbf{r}, \mathbf{r}') = -\frac{\delta u(\mathbf{r}')}{\delta\rho(\mathbf{r})}. \tag{5}$$

This means that the softness kernel and the hardness kernel are inverses of each other, i.e.

$$\mathbf{s} = \boldsymbol{\eta}^{-1}. \tag{6}$$

Then, the local softness $s(\mathbf{r})$ is defined as:

$$s(\mathbf{r}) = \int s(\mathbf{r}, \mathbf{r}')\mathrm{d}\mathbf{r}' = 1^{\top}\mathbf{s} = 1^{\top}\boldsymbol{\eta}^{-1} \tag{7}$$

and the global softness S is defined as:

$$S = \int s(\mathbf{r})\mathrm{d}\mathbf{r} = 1^{\top}\mathbf{s}1 = 1^{\top}\boldsymbol{\eta}^{-1}1. \tag{8}$$

Now putting equations (6)–(8) into equation (1), we get the expression of CRK in matrix form:

$$\boldsymbol{\chi} = -\boldsymbol{\eta}^{-1} + \frac{\boldsymbol{\eta}^{-1}1 \otimes 1^{\top}\boldsymbol{\eta}^{-1}}{1^{\top}\boldsymbol{\eta}^{-1}1}. \tag{9}$$

The expression above is a key relation in the conceptual DFT, which will naturally reappear in the CPE method [58] as also derived from the conceptual DFT. It is worth noting that because of the derivative discontinuity of the energy [67], the interpretation of the hardness kernel would need a finite-temperature perspective [68]. However, no such difficulty is posed for the CRK $\boldsymbol{\chi}$ or the softness kernel $\mathbf{s}$.

In addition, it is worth noting that the global softness S (therefore the hardness matrix $\boldsymbol{\eta}$) is directly linked to the fundamental gap E_{g} of the system (as the difference between the ionization potential I and the electron affinity A) [69] via the finite-difference approximation, i.e.

$$E_{\mathrm{g}} = I - A \approx S^{-1} = \frac{1}{1^{\top}\boldsymbol{\eta}^{-1}1}. \tag{10}$$

2.2. Charge response kernel and dielectric functions

In solid state physics [63], CRK plays an equally important role. The idea is to introduce the screened potential $\delta\varphi(\mathbf{r})$, which is the overall potential change induced by the external potential $\delta\nu(\mathbf{r})$ via the potential kernel $\nu(\mathbf{r} - \mathbf{r}')$, as

$$\delta\varphi(\mathbf{r}) = \delta\nu(\mathbf{r}) + \int \mathrm{d}\mathbf{r}' \int \mathrm{d}\mathbf{r}''\, \nu(\mathbf{r} - \mathbf{r}')\chi(\mathbf{r}', \mathbf{r}'')\delta\nu(\mathbf{r}''). \tag{11}$$

Then, this leads to the definition of a dielectric function $\epsilon(\mathbf{r}, \mathbf{r}')$ by:

$$\delta\varphi(\mathbf{r}) = \int \mathrm{d}\mathbf{r}'\, \epsilon^{-1}(\mathbf{r}, \mathbf{r}')\delta\nu(\mathbf{r}'), \tag{12}$$

where $\epsilon(\mathbf{r}, \mathbf{r}')$ is expressed as:

$$\epsilon^{-1}(\mathbf{r}, \mathbf{r}') = \delta(\mathbf{r} - \mathbf{r}') + \int \mathrm{d}\mathbf{r}''\, \nu(\mathbf{r} - \mathbf{r}'')\chi(\mathbf{r}', \mathbf{r}''). \tag{13}$$

Also, one can introduce the so-called irreducible response function $\chi_0(\mathbf{r}, \mathbf{r}')$ as

$$\chi_0(\mathbf{r}, \mathbf{r}') = \frac{\delta\rho(\mathbf{r})}{\delta\varphi(\mathbf{r}')}. \tag{14}$$

The connection between χ_0 and χ is [63]:

$$\chi(\mathbf{r}, \mathbf{r}') = \int \mathrm{d}\mathbf{r}''\, \chi_0(\mathbf{r}, \mathbf{r}'')\epsilon^{-1}(\mathbf{r}'', \mathbf{r}'). \tag{15}$$

Now writing the above formula in matrix form, one has:

$$\boldsymbol{\chi} = \boldsymbol{\chi}_0\boldsymbol{\epsilon}^{-1}. \tag{16}$$

Accordingly, equation (13) can be rewritten as:

$$\boldsymbol{\epsilon}^{-1} = \mathbf{I} + \mathbf{V}\boldsymbol{\chi}. \tag{17}$$

Substituting equation (17) into equation (16), we got:

$$\boldsymbol{\chi} = \left[\mathbf{I} - \boldsymbol{\chi}_0\mathbf{V}\right]^{-1}\boldsymbol{\chi}_0. \tag{18}$$

Applying the push-through identity $(\mathbf{I}+\mathbf{UL})^{-1}\mathbf{U}=\mathbf{U}(\mathbf{I}+\mathbf{LU})^{-1}$ to equation (18), one gets:

$$\boldsymbol{\chi}=\boldsymbol{\chi}_0\left[\mathbf{I}-\mathbf{V}\boldsymbol{\chi}_0\right]^{-1}. \tag{19}$$

This is so-called Dyson's equation, which is widely used to compute photo-emission spectra (GW calculations [70]) and adsorption spectra as well as to include the long-range correlation effects (e.g. RPA correlation energies [71]).

As the consequence of equation (19), the dielectric matrix $\boldsymbol{\epsilon}$ can be expressed as:

$$\boldsymbol{\epsilon}=\mathbf{I}-\mathbf{V}\boldsymbol{\chi}_0. \tag{20}$$

2.3. Charge response kernel and chemical potential equalization

The CRK and the CPE method are closely related, as mentioned at the beginning and outlined in this section. The starting point is the Euler–Lagrange equation for the ground-state system under the perturbation of an external potential $\delta\nu(\mathbf{r})$ [58]:

$$\int\eta(\mathbf{r},\mathbf{r}')\delta\rho(\mathbf{r}')\mathrm{d}\mathbf{r}'+\delta\nu(\mathbf{r})=\mu-\mu_0, \tag{21}$$

where $\delta\rho(\mathbf{r})$ is the density response to the external potential $\delta\nu(\mathbf{r})$, μ is the chemical potential of the perturbed system, and μ_0 is the chemical potential of the unperturbed system. This expression comes from the expansion of the energy up to the second order of $\delta\rho(\mathbf{r})$ and $\delta\nu(\mathbf{r})$ [72].

In the work of York and Yang [58], equation (21) was transformed into an algebraic equation, which is the core of the CPE method and reminiscent of the EEM from Mortier *et al* [49, 50] and the QEq of Rappé and Goddard [51].

In CPE, the electronic energy of the system is given by:

$$\mathcal{U}(\mathbf{c})=\mathcal{U}_0+\langle\rho_0|\delta\nu\rangle+\mu_0\mathbf{1}^\top\mathbf{c}+\Delta\boldsymbol{\nu}^\top\mathbf{c}+\frac{1}{2}\mathbf{c}^\top\boldsymbol{\eta}\mathbf{c}, \tag{22}$$

where $\mathcal{U}_0$ is the electronic energy of the unperturbed system and the coefficient $\mathbf{c}$ comes from the expansion of the density response $\delta\rho(\mathbf{r})$ (with respect to the ground-state density $\rho_0(\mathbf{r})$) in basis functions ϕ_i as:

$$\delta\rho(\mathbf{r})=\sum_i c_i\phi_i(\mathbf{r}) \tag{23}$$

and one commonly used type of basis functions is the s-type Gaussian function

$$\phi_i(\mathbf{r})=\left(\frac{\zeta_i}{\pi}\right)^{3/2}\exp^{-\zeta_i|\mathbf{r}-\mathbf{R}_i|^2}. \tag{24}$$

Applying the variational principle, the coefficient $\mathbf{c}$ can be found by solving the following set of equations for a system of N_0 number of electrons:

$$\frac{\partial}{\partial\mathbf{c}}\left\{\mathcal{U}(\mathbf{c})-\mu\mathbf{1}^\top\mathbf{c}\right\}=0 \tag{25}$$

with the charge conservation constraint $\mathbf{1}^\top\mathbf{c}=0$.

The solution of equation (25) is:

$$\mathbf{c}=-\left(\boldsymbol{\eta}^{-1}-\frac{\boldsymbol{\eta}^{-1}\mathbf{1}\otimes\mathbf{1}^\top\boldsymbol{\eta}^{-1}}{\mathbf{1}^\top\boldsymbol{\eta}^{-1}\mathbf{1}}\right)\Delta\boldsymbol{\nu}. \tag{26}$$

Comparing it to equation (9), one can immediately see that the solution of the CPE method can be simply rewritten as the product of the atom-condensed CRK and the external potential $\Delta\boldsymbol{\nu}$:

$$\mathbf{c}=\boldsymbol{\chi}\Delta\boldsymbol{\nu}. \tag{27}$$

In the CPE method, $\Delta\boldsymbol{\nu}$ is a perturbation in the external potential evaluated with the chosen basis function, which naturally leads to the definition of $\boldsymbol{\chi}$ and the response charge $\mathbf{c}$. Despite of the mathematical similarity [73], $\Delta\boldsymbol{\nu}$ is conceptually different from the atomic electronegativity $\mathbf{b}$ used in obtaining the atomic charge $\mathbf{q}_0$ [74].

2.4. Charge response kernel and ACKS2

Atom-condensed Kohn–Sham DFT ACKS2 [59] is a recently developed method which attempted to better approximate the hardness matrix $\boldsymbol{\eta}$ by separating the contribution of the Kohn–Sham kinetic energy T_s from the rest terms:

$$\eta(\mathbf{r},\mathbf{r}') = \nu(\mathbf{r},\mathbf{r}') + \frac{\delta^2 T_s}{\delta\rho(\mathbf{r})\delta\rho(\mathbf{r}')}, \tag{28}$$

where the potential kernel $\nu(\mathbf{r},\mathbf{r}')$ in the Kohn–Sham DFT contains contributions from the Hartree potential ν_H and the exchange-correlation potential ν_{xc} as

$$\nu(\mathbf{r},\mathbf{r}') = \frac{\delta\nu_H(\mathbf{r})}{\delta\rho(\mathbf{r}')} + \frac{\delta\nu_{xc}(\mathbf{r})}{\delta\rho(\mathbf{r}')}. \tag{29}$$

This is achieved by taking the EEM ansatz for constructing $\boldsymbol{\eta}_e$ (see section 3.2) and introducing the non-interacting linear response kernel $\boldsymbol{\chi}_s$, i.e.

$$\chi_s(\mathbf{r},\mathbf{r}') = \left[\frac{\delta\rho(\mathbf{r})}{\delta\nu_{KS}(\mathbf{r}')}\right]_{N_0}, \tag{30}$$

where ν_{KS} is the Kohn–Sham effective potential.

In the original representation of ACKS2, the kinetic energy contribution is accessed by formulating it as a constrained optimization problem and solving it with the Lagrange multiplier method in the form of block matrix:

$$\begin{bmatrix} \boldsymbol{\eta}_e & -1 & -\mathbf{I} & 0 \\ -1^\top & 0 & 0 & 0 \\ -\mathbf{I} & 0 & \boldsymbol{\chi}_s & -1 \\ 0 & 0 & -1^\top & 0 \end{bmatrix} \begin{bmatrix} \mathbf{c} \\ \mu \\ \boldsymbol{\varphi} \\ \lambda_u \end{bmatrix} = \begin{bmatrix} -\Delta\boldsymbol{\nu} \\ 0 \\ 0 \\ 0 \end{bmatrix}, \tag{31}$$

where $\boldsymbol{\varphi}$ is the auxiliary Kohn–Sham potential and λ_u is the corresponding Lagrangian multiplier.

The non-interacting linear response kernel $\boldsymbol{\chi}_s$ in the Kohn–Sham theory [75] is defined exactly in the same way as the irreducible response function $\boldsymbol{\chi}_0$ introduced in equation (14) and $\boldsymbol{\eta}_e$ represents the remaining part of the hardness kernel by excluding the contribution from the kinetic energy (equation (28)). Thus, as shown in the proof in the appendix A, one can construct the CRK in ACKS2 via Dyson's equation (equation (19)) by identifying $\boldsymbol{\chi}_s \leftrightarrow \boldsymbol{\chi}_0$ and $\boldsymbol{\eta}_e \leftrightarrow \mathbf{V}$. Subsequently, the solution of equation (31) in ACKS2 can be readily obtained by inserting the expression of $\boldsymbol{\chi}$ as follows into equation (27):

$$\boldsymbol{\chi} = \boldsymbol{\chi}_s\left[\mathbf{I} - \boldsymbol{\eta}_e\boldsymbol{\chi}_s\right]^{-1}. \tag{32}$$

2.5. Charge response kernel and molecular polarizability

The importance of the CRK $\boldsymbol{\chi}$ lies in the fact that it is not only connected to CPE and ACKS2 methods but also linked to the molecular polarizability, as discussed in this section.

The negative of $\boldsymbol{\chi}$ is equal to the charge susceptibility $a(\mathbf{r},\mathbf{r}')$ as shown by Stone [76], and the corresponding molecular polarizability component α_{ab} can be expressed in terms of CRK as

$$\alpha_{ab} = \iint \mathrm{d}\mathbf{r}\,\mathrm{d}\mathbf{r}' r_a a(\mathbf{r},\mathbf{r}') r'_b. \tag{33}$$

In matrix form, the above expression for the atom-condensed $\boldsymbol{\chi}$ (expressed in terms of s-type Gaussian function, i.e. equation (23)) can be written as

$$\boldsymbol{\alpha} = \mathbf{R}^\top \boldsymbol{a}\mathbf{R} = -\mathbf{R}^\top\boldsymbol{\chi}\mathbf{R}. \tag{34}$$

The above representation of molecular polarizability has the characteristic of being rotational covariant, translational invariant and permutational invariant, in which $\boldsymbol{\chi}$ itself is a scalar function. Its rotational covariance comes out by construction. The translational and permutational invariance of equation (34) will be elaborated in the following.

Any translation of the system can be written as

$$\mathbf{T} = 1 \otimes [d_1, d_2, d_3], \tag{35}$$

where d_i is the translational distance. Therefore, because of the sum rule presented in equation (3), one can show that

$$[\mathbf{R}+\mathbf{T}]^\top\boldsymbol{\chi}[\mathbf{R}+\mathbf{T}] = \mathbf{R}^\top\boldsymbol{\chi}\mathbf{R} \tag{36}$$

thus the polarizability expressed in equation (34) is translationally invariant.

A permutation of the atoms of the system can be represented as an $N \times N$ permutation matrix $\mathbf{P}$. This results in

$$(\mathbf{PR})^\top(\mathbf{P}\boldsymbol{\chi}\mathbf{P}^\top)\mathbf{PR} = \mathbf{R}^\top\mathbf{P}^\top\mathbf{P}\boldsymbol{\chi}\mathbf{P}^\top\mathbf{PR} = \mathbf{R}^\top\boldsymbol{\chi}\mathbf{R}, \tag{37}$$

where we have used the fact that $\mathbf{P}^\top\mathbf{P} = \mathbf{I}$ for any permutation matrix. This means that the polarizability expressed in equation (34) is also permutational invariant.

2.6. Finite-field (potential) coupling via charge response kernel

The finite-field (potential) coupling can be introduced straightforwardly once the CRK of the system is known.

Under an external field $\mathbf{E}_0$, the CPE equation can be expanded as

$$\mathcal{U}(\mathbf{c}, \mathbf{E}_0) = \mathcal{U}_0 + \langle\rho_0|\delta\nu\rangle + \mu_0 1^\top\mathbf{c} + \Delta\boldsymbol{\nu}^\top\mathbf{c} + \frac{1}{2}\mathbf{c}^\top\boldsymbol{\eta}\mathbf{c} - \mathbf{E}_0^\top\mathbf{R}^\top(\mathbf{c} + \mathbf{q}_0). \tag{38}$$

Here $\mathbf{R}^\top(\mathbf{c} + \mathbf{q}_0)$ provides the dipole moment in the system for the usage of the s-type Gaussian function as basis function (equation (23)), and $\mathbf{q}_0$ is the atomic charge of the unperturbed system.

Similarly to the previous case, applying the variational principle leads to the following set of equations for a system of N_0 number of electrons:

$$\frac{\partial}{\partial\mathbf{c}}\left\{\mathcal{U}(\mathbf{c}, \mathbf{E}_0) - \mu 1^\top\mathbf{c}\right\} = 0 \tag{39}$$

with the charge conservation constraint $\mathbf{1}^\top\mathbf{c} = 0$.

The solution of equation (39) gives the response charge:

$$\mathbf{c} = -\left(\boldsymbol{\eta}^{-1} - \frac{\boldsymbol{\eta}^{-1}1 \otimes 1^\top\boldsymbol{\eta}^{-1}}{1^\top\boldsymbol{\eta}^{-1}1}\right)(\Delta\boldsymbol{\nu} - \mathbf{R}\mathbf{E}_0). \tag{40}$$

Therefore, the response charge under the external field $\mathbf{E}_0$ can be expressed again in terms of the CRK.

$$\mathbf{c} = \boldsymbol{\chi}(\Delta\boldsymbol{\nu} - \mathbf{R}\mathbf{E}_0). \tag{41}$$

The case of finite potential $\boldsymbol{\Psi}$ coupling can be implemented in a similar fashion, where the coupling term in equation (38) is $\boldsymbol{\Psi}^\top(\mathbf{c} + \mathbf{q}_0)$ instead.

3. Learning the charge response kernel

The CRK can be learned using local descriptors to reproduce the molecular polarizability via equation (34). The requirement for constructing the atom-condensed CRK is two-fold (i) the symmetric property $\boldsymbol{\chi} = \boldsymbol{\chi}^\top$; (ii) the sum rule $\mathbf{1}^\top\boldsymbol{\chi} = \mathbf{0}$.

As illustrated in figure 1, different strategies can be used to approximate $\boldsymbol{\chi}$ utilizing ML predictions. Without loss of generality, we present here three types of models, namely the Local-, EtaInv- and ACKS2-type models, by showing how $\boldsymbol{\chi}$ is constructed from ML predictions in the form of atomic properties $\mathbb{P}_i$ and pairwise interactions $\mathbb{I}_{ij}$ in PiNet. To put this comparison into perspective, we also introduce here a baseline model (the EEM-type model). Before that, we will first briefly introduce the architecture of PiNet.

3.1. PiNet-χ framework

Training and prediction of the CRK was performed with PiNet, a GCNN implemented in the open source atomic neural network Python library PiNN [62]. In PiNet, the atomic properties $\mathbf{P}_i$ form the nodes and the pairwise interactions $\mathbf{I}_{ij}$ form the weighted edges of the graph, both being iteratively updated as latent variables. In the original version of PiNet, outputs are generated as atomic predictions $\mathbb{P}_i$. Here, we used PiNet to generate both types of predictions $\mathbb{P}_i$ and their pairwise interactions $\mathbb{I}_{ij}$ to construct the matrix elements in η_e, $\boldsymbol{\eta}^{-1}$, $\boldsymbol{\chi}_i$ or $\boldsymbol{\chi}_s$ (see figure 1 and section 2 for theory and methods).

The architecture of PiNet can be described as an iteration over graph convolution blocks, which consist of three neural networks and an interaction pooling operation (see algorithm 1). This allows the network to generate descriptors automatically without any hand-crafting [62]. The iterative graph convolution means that atomic and interaction properties are gathered from atoms within a distance $n_{GC} \cdot r_c$, where n_{GC} is the number of graph convolution iterations and r_c is the neighbour cut-off radius.

PiNet takes a one-hot encoding of the atoms $\mathbf{P}_i^0$ and n_b Gaussian basis functions $\mathbf{e}_{ij}$ as input. In each graph convolution block, the $\mathrm{NN}^{\mathrm{PI}}$ (property to interaction) network takes vectors $\mathbf{P}_i$, $\mathbf{P}_j$ as input, and outputs a weight matrix $\mathbf{W}_{ij}$ for each basis function $\mathbf{e}_{ij}$; the $\mathrm{NN}^{\mathrm{II}}$ (interaction to interaction) network then forms the

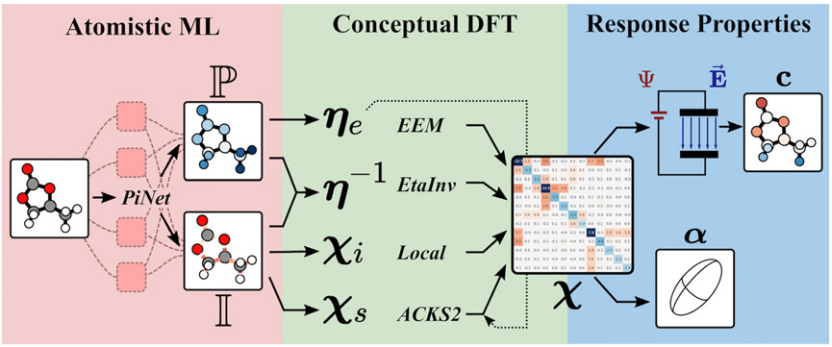

Figure 1. Schematic illustration of the PiNet-χ framework for predicting response properties. Different types of models (EEM, EtaInv, Local and ACKS2) rooted in conceptual DFT are taken to describe the atom-condensed CRK $\boldsymbol{\chi}$ from the ML predictions of atomic properties $\mathbb{P}$ and pairwise interactions $\mathbb{I}$ using the neural network architecture PiNet. $\boldsymbol{\chi}$ is a central quantity to generate response properties, such as molecular polarizability $\boldsymbol{\alpha}$ and response charges $\mathbf{c}$.

Algorithm 1. PiNet iterative graph convolution, where NN stands for feed-forward neural networks; IP stands for the interaction pooling operation; $\mathbf{P}_i^t$, $\tilde{\mathbf{P}}_i^t$, $\mathbf{I}_{ij}^t$ and $\mathbf{W}_{ij}^t$, are the atomistic property, the intermediate atomistic property, the pairwise interaction and the weight matrix at each iteration; $\mathbb{P}_i$ and $\mathbb{I}_{ij}$ are the final, scalar property and interaction predictions.

Input: n_{GC}—*number of GC-blocks*
$\mathbf{P}_i^0$—*atomic one-hot encoding*
$\mathbf{e}_{ij}$—*vector of basis functions for interactions* i, j
PiNet$(n_{\mathrm{GC}}, \mathbf{P}_i^0, \mathbf{e}_{ij})$
  for $t = 1$ to n_{GC}
  $\mathbf{W}_{ij}^t = \mathrm{NN}^{\mathrm{PI}}(\mathbf{P}_i^{t-1}, \mathbf{P}_j^{t-1})$
  $\mathbf{I}_{ij}^t = \mathrm{NN}^{\mathrm{II}}(\mathbf{W}_{ij}^t \mathbf{e}_{ij})$
  $\tilde{\mathbf{P}}_i^t = \mathrm{IP}\left(\sum_j \mathbf{I}_{ij}^t, \mathbf{P}_i^{t-1}\right)$
  $\mathbf{P}_i^t = \mathrm{NN}^{\mathrm{PP}}(\tilde{\mathbf{P}}_i^t)$
  $\mathbb{P}_i = \sum_t \mathrm{NN}_{\mathrm{out}}^{\mathrm{PP}}(\tilde{\mathbf{P}}_i^t)$
  $\mathbb{I}_{ij} = \mathbf{e}_{ij} \cdot \sum_t \mathrm{NN}_{\mathrm{out}}^{\mathrm{PI}}(\tilde{\mathbf{P}}_i^t, \tilde{\mathbf{P}}_j^t)$
  return $\mathbb{P}_i, \mathbb{I}_{ij}$

interaction vector $\mathbf{I}_{ij}$ from the weighted basis functions $\mathbf{W}_{ij}\mathbf{e}_{ij}$. The interactions $\mathbf{I}_{ij}$ are summed into the intermediate property vector $\tilde{\mathbf{P}}_i$ through an IP (interaction pooling) operation akin to the skip connection in ResNet [77]. $\tilde{\mathbf{P}}_i$ is used to update the $\mathbf{P}_i$ vector through the $\mathrm{NN}^{\mathrm{PP}}$ (property to property) network, and to generate the outputs $\mathbb{P}_i$ and $\mathbb{I}_{ij}$ through the output networks $\mathrm{NN}_{\mathrm{out}}^{\mathrm{PP}}$ and $\mathrm{NN}_{\mathrm{out}}^{\mathrm{PI}}$.

3.2. EEM-type model

In the conventional EEM approximation of $\boldsymbol{\eta}$ by $\boldsymbol{\eta}_{\mathrm{e}}$, the hardness matrix includes an on-site atomic hardness parameter and the Coulomb kernel due to electrostatic interactions. In our implementation, we introduce a set of environment-dependent on-site parameters $\mathbb{P}_i$ as follows

$$(\eta_{\mathrm{e}})_{ii} = \mathbb{P}_i + \sqrt{\frac{2\zeta_i}{\pi}}$$
$$(\eta_{\mathrm{e}})_{ij} = \frac{\mathrm{erf}\left(R_{ij}\sqrt{\frac{\zeta_i\zeta_j}{\zeta_i+\zeta_j}}\right)}{R_{ij}} \quad \text{for } i \neq j, \tag{42}$$

where $\mathbb{P}_i$ are the atomic predictions from PiNet, depending on the local chemical environment (see table S1 (https://stacks.iop.org/EST/4/014012/mmedia) in the ESI). The parameters ζ_i are optimized during training (see table S2 in the ESI).

3.3. Local-type model

Our local-type model is related to the idea of predicting the polarizability tensor through atomic contributions $\boldsymbol{\alpha}_i$ [37, 38]. In our implementation, we construct $\boldsymbol{\alpha}_i$ from bond vectors using their tensor product to ensure

the translational and rotational invariance of the prediction:

$$\boldsymbol{\alpha} = \sum_i \boldsymbol{\alpha}_i = \sum_i \left(\sum_j \mathbb{I}_{ij} \cdot \mathbf{r}_{ij} \right)^\top \otimes \left(\sum_j \mathbb{I}_{ij} \cdot \mathbf{r}_{ij} \right), \tag{43}$$

where $\mathbb{I}_{ij}$ is a pairwise scalar prediction between atoms i and j from the neural network. Here we show that an atom-centered $\boldsymbol{\chi}_i$ can be obtained by rearranging equation (43) in a matrix form:

$$\boldsymbol{\alpha}_i = \left(\mathbb{I}_i^\top \boldsymbol{\Delta}_i \mathbf{R}\right)^\top \otimes \left(\mathbb{I}_i^\top \boldsymbol{\Delta}_i \mathbf{R}\right) = \mathbf{R}^\top \left(\boldsymbol{\Delta}_i^\top \mathbb{I}_i \mathbb{I}_i^\top \boldsymbol{\Delta}_i\right) \mathbf{R} = -\mathbf{R}^\top \boldsymbol{\chi}_i \mathbf{R} \tag{44}$$

$$\boldsymbol{\chi}_i = -\boldsymbol{\Delta}_i^\top \mathbb{I}_i \mathbb{I}_i^\top \boldsymbol{\Delta}_i, \tag{45}$$

where $\boldsymbol{\Delta}_i = \mathbf{I} - 1 \otimes \mathbf{e}_i^\top$ can be intuitively understood as an operator converting atomic coordinates to bond vectors starting from i with $\mathbf{e}_i$ being the ith standard unit vector, and $\mathbb{I}_i$ is the vector of size N denoting the interaction predictions centering on the atom i. It is easy to verify that $\boldsymbol{\chi}_i$ and $\boldsymbol{\chi}$ fulfil equations (2) and (3).

3.4. EtaInv-type model

In our EtaInv-type model, the aim is to construct $\boldsymbol{\chi}$ by predicting directly the softness matrix $\boldsymbol{\eta}^{-1}$. This model has the advantage that no matrix inversion operation is involved.

To ensure the positive definiteness of $\boldsymbol{\eta}^{-1}$, we introduce the following form

$$\boldsymbol{\eta}^{-1} = \mathbf{B}^\top \mathbf{B} + c\mathbf{I}, \tag{46}$$

where $\mathbf{B}$ is the predicted matrix

$$\begin{aligned} B_{ii} &= \mathbb{P}_i \\ B_{ij} &= \mathbb{I}_{ij} \quad \text{for } i \neq j \end{aligned} \tag{47}$$

and $c > 0$ is a small constant. The positive definiteness of this form is made clear from noting that the eigenvalues λ are defined by

$$(\mathbf{B}^\top \mathbf{B} + c\mathbf{I})\mathbf{v} = \lambda \mathbf{v} \tag{48}$$

and from the relation

$$\mathbf{v}^\top \mathbf{B}^\top \mathbf{B} \mathbf{v} = (\lambda - c)\mathbf{v}^\top \mathbf{v}, \tag{49}$$

all eigenvalues fulfil $\lambda \geqslant c$. A rank-1 update to $\boldsymbol{\eta}^{-1}$ then gives the $\boldsymbol{\chi}$ matrix following equation (9).

3.5. ACKS2-type model

As we have shown in equation (32), $\boldsymbol{\chi}$ in ACKS2 model can be written in terms of $\boldsymbol{\chi}_\mathrm{s}$ and $\boldsymbol{\eta}_\mathrm{e}$. Therefore, the ML task is to predict $\boldsymbol{\chi}_\mathrm{s}$ and $\boldsymbol{\eta}_\mathrm{e}$.

In our implementation, we construct $\boldsymbol{\chi}_\mathrm{s}$ as a local and trainable matrix, by taking a symmetrized pairwise prediction $\mathbb{I}$ (a sparse matrix with dimension $N \times N$) and adjust the diagonal terms to enforce the sum rule:

$$\boldsymbol{\chi}_\mathrm{s} = |\mathbb{I}| + |\mathbb{I}|^\top - \mathrm{diag}\left(|\mathbb{I}|1 + |\mathbb{I}|^\top 1\right). \tag{50}$$

The $\boldsymbol{\eta}_\mathrm{e}$ matrix in the ACKS2 is constructed from the atomic prediction $\mathbb{P}$ as in the EEM formalism (equation (42)), where ζ are again trainable parameters.

When setting $\boldsymbol{\eta}_\mathrm{e} = \mathbf{0}$, this leads to $\boldsymbol{\chi} = \boldsymbol{\chi}_\mathrm{s}$. Therefore, equation (50) also provides a means for directly constructing $\boldsymbol{\chi}$.

4. Dataset, model training and reference calculations

4.1. Description of dataset

In this work, the training of PiNet-χ models were performed using the polarizability tensors from the QM7b dataset, which consists of 7211 organic molecules [78]. The dipole polarizabilities computed using the B3LYP functional [79] and the d-Aug-cc-pVDZ basis set [80] were used here. Note that this dataset contains also HOMO–LUMO orbital energies, which will be used in the results and discussion section.

To obtain the thickness-resolved root mean square error (RMSE), we define the molecular thickness using the singular value decomposition of $\mathbf{R}^\top \mathbf{R}$.

$$\left(\mathbf{R}^\top \mathbf{R}\right) = \mathbf{v}\boldsymbol{\Sigma}\mathbf{v}^\top = \mathbf{v} \begin{bmatrix} \sigma_x^2 & 0 & 0 \\ 0 & \sigma_y^2 & 0 \\ 0 & 0 & \sigma_z^2 \end{bmatrix} \mathbf{v}^\top,$$

Table 1. Specifications used to train PiNet-χ models. Here the layer architectures are denoted by the number of nodes for the hidden layers and the output layer. The parameters r_c, n_{GC}, n_b and γ indicate the cut-off radius, the number of graph-convolution blocks, the number of radial basis functions for each (i, j) tuple and the basis function Gaussian width respectively.

Layer	Architecture	Parameter	Value
PI	$[32 \times n_b]$	r_c	4.5 Å
II	[32, 32, 32, 32]	n_{GC}	5
PP	[32, 32, 32, 32]	n_b	20
PI_{out}	$[32, 1 \times n_b]$	γ	3 $Å^{-2}$
PP_{out}	[32, 1]		

where $\mathbf{v}^{-1} = \mathbf{v}^{\top}$. With this, $\mathbf{v}$ can be regarded as a rotation matrix which yields the covariance of positions as a diagonal matrix. For planar molecules, $\sigma_z^2 = 0$. Thus, σ_z^2 yields a measure of thickness for the other molecules.

4.2. Loss function and error metrics

All four types of CRK model (EEM, Local, EtaInv, and ACKS2) provide the polarizability predictions, with which the RMSE of polarizability per atom may be defined through the Frobenius norm of the error:

$$\mathrm{RMSE} = \sqrt{\frac{1}{N}\sum_i || \boldsymbol{\alpha}_i^{\mathrm{data}} - \boldsymbol{\alpha}_i^{\mathrm{pred}} ||_{\mathrm{F}}^2 / n_i^2}. \tag{51}$$

In the present work, this per atom RMSE was used as the loss function. Further, the RMSE can be separated to the contributions of isotropic polarizability and anisotropic one [37]:

$$\mathrm{RMSE}_{\mathrm{iso}} = \sqrt{\mathrm{RMSE}^2 - \mathrm{RMSE}_{\mathrm{aniso}}^2}. \tag{52}$$

4.3. Hyperparameters

The network architecture used in PiNet-χ is listed in table 1, which specifies the number of nodes in the hidden layers and the output layer, the cut-off radius, the number of graph-convolution blocks, the number of radial basis functions and the corresponding Gaussian width.

4.4. Model training

Model training was performed with 80% of the QM7 data set, leaving 20% as a validation set. Ten instances of each model type were trained, each with different random seeds to determine the data set split. The TensorFlow [81] implementation of the Adam optimizer [82] was used for 5×10^5 gradient descent steps with a mini-batch size of 30. The initial learning rate was set to 3×10^{-4} and an exponential decay schedule was used to decrease the learning rate by a factor of 0.994 every 10^4 steps. To avoid exploding gradient problems [83], gradient norm clipping was applied.

4.5. Reference calculations for the response charge

The reference calculations for the example molecules (propylene carbonate, acetonitrile, methanol and DMSO) were carried out using the same settings as the QM7b dataset and with the Gaussian09 software [84]. The Merz–Singh–Kollman (MSK) charges [85, 86] were computed for a set of different electric field strengths applied in the z-direction. For all these calculations, the dipole moment and the electron density were saved as well. The response charge and charge density were obtained by subtracting those obtained at a field strength of zero.

Computations for the graphene flake were done in a similar fashion, although using the cc-pVDZ basis set because of the system size [80]. First, the electronic structure of the graphene flake were computed without any external perturbation. Then another calculation was done with the addition of a point charge of $+1e$ added 2.5 Å above the centre of the graphene flake. In addition to the MSK charge, the Mulliken [87] and Hirshfeld [88] charges were also recorded.

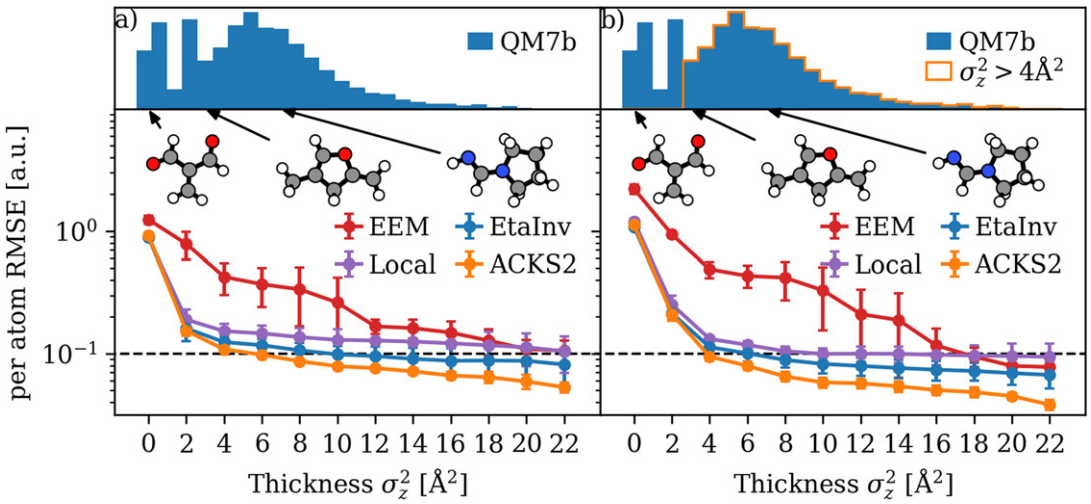

Figure 2. Thickness-resolved RMSE of PiNet-χ models for predicting molecular polarizability $\boldsymbol{\alpha}$, trained on (a) the entire QM7b dataset and (b) filtered training sets with non-planar molecules. The thickness distributions of the entire QM7b dataset and molecules with $\sigma_z^2 > 4$ Å^2 are shown in the upper panels. The validation RMSE are plotted against the thickness threshold in the lower panels, where molecules with thickness below the given threshold are excluded.

Table 2. Errors metrics of PiNet-χ models for polarizability tensor $\boldsymbol{\alpha}$ predictions in the QM7b dataset. All models were trained on 80% of the entire QM7b dataset, while the model evaluation was done on the remaining data filtered by excluding molecules with a thickness σ_z^2 smaller than 4 Å^2 (see section 4.1 for details regarding the definition of thickness σ_z^2). Results of each model were averaged over 10 training instances. Errors are presented as RMSE (a.u.) for the full tensor as well as its isotropic and anisotropic parts. These values are all given on the 'per atom' basis.

Model	RMSE	RMSE_{iso}	$\text{RMSE}_{\text{aniso}}$
EEM	0.4 (1)	0.3 (1)	0.33 (8)
Local	0.15 (2)	0.10 (3)	0.12 (1)
EtaInv	0.12 (1)	0.07 (2)	0.102 (6)
ACKS2	0.11 (1)	0.07 (1)	0.086 (6)

5. Results and discussion

5.1. Prediction of molecular polarizability

Since $\boldsymbol{\chi}$ in this work is constructed by reproducing molecular polarizability, it is mandatory to see how well PiNet-χ predicts $\boldsymbol{\alpha}$. However, there is one issue which needs to be taken care of before showing these results.

In our scheme, the molecular polarizability $\boldsymbol{\alpha}$ is computed from $\boldsymbol{\chi}$ using equation (34). In spite of desired features of $\boldsymbol{\chi}$, such as translational, rotational and permutational invariance, this also means that any planar molecular described using only s-type basis function for the response-charge density would lead to zero component in $\boldsymbol{\alpha}$ (because of the condition imposed by equation (3)). Therefore, it is necessary to show how the model accuracy changes with respect to the thickness of the molecule. Here the thickness is defined as the single value component σ_z^2 generated from the singular value decomposition of the positional co-variance matrix of each molecule (see details in section 4.1). For a single planary molecule, e.g. benzene, σ_z^2 is strictly zero. However, two parallel-displaced benzene rings would have a non-zero value of σ_z^2. That is the reason why we call σ_z^2 'thickness' instead of 'planarity' in this context.

Results of the thickness-resolved RMSE for predicting $\boldsymbol{\alpha}$ in QM7b dataset are then shown in figure 2(a), where all numbers are 'per atom' values. As expected, the performance of the PiNet-χ models gets significantly better for molecules having a thickness larger than 4 Å^2. The corresponding error metrics of all types of PiNet-χ models at σ_z^2 of 4 Å^2 are listed in table 2 and parity plots are provided in figure S1 in the ESI.

From both figure 2(a) and table 2, it is clear that Local-type, EtaInv-type and ACKS2-type models perform significantly better for predicting the polarizability, compared to the EEM-type model. Among these three, the ACKS2-type model shows the best accuracy for both isotropic and anisotropic components of the polarizability tensor, with an RMSE below 0.1 a.u. per atom. To put this number into perspective, it is worthwhile noting

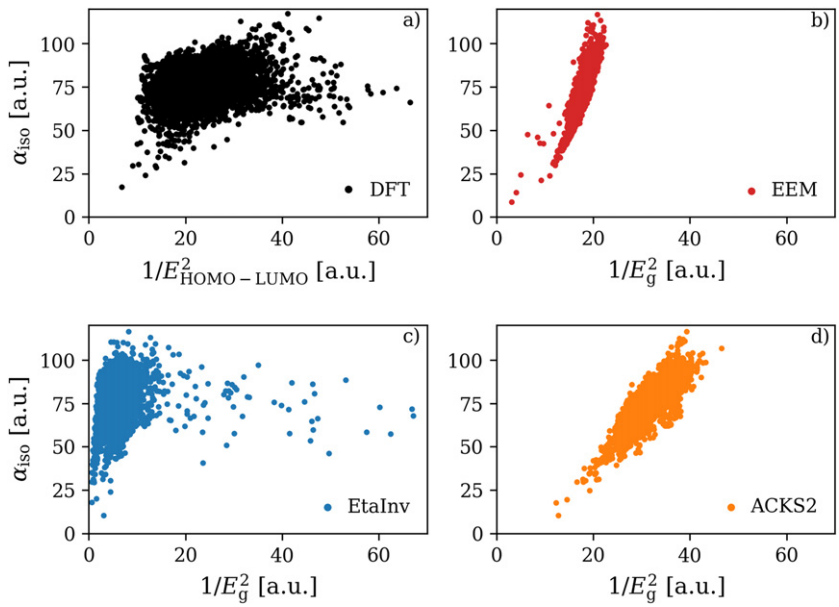

Figure 3. Correlation between the isotropic polarizability and the energy gap for the QM7b dataset. (a) α_{iso} versus $1/E^2_{HOMO-LUMO}$; (b)–(d): α_{iso} versus $1/E^2_g$ using equation (10) for EEM, EtaInv and ACKS2 types of models. In the case of EEM and ACKS2, $\boldsymbol{\eta}$ is substituted with $\boldsymbol{\eta}_e$.

that the RMSE error of isotropic polarizability for small molecules of 2 to 13 atoms using hybrid functionals with respect to experimental values is about 2 a.u. [89].

Then, we also tested whether filtering out planar molecules in the training set would help to improve the model accuracy or not. For this purpose, molecules in the training set with thickness σ_c^2 smaller than 4 Å^2 were excluded. The corresponding result is shown in figure 2(b). As one can see, filtering out planar molecules in the training set does slightly improve the model prediction and lower the corresponding RMSE. However, the general trends among different PiNet-χ models remain the same. Therefore, all results shown in the following sections were based on PiNet-χ models trained with the entire QM7b dataset without any filtering.

To see how PiNet-χ models perform outside the QM7b distribution, we also used a subset of the Bosque–Sales (BS) dataset (see figure S2 for the details), which contains 242 solvent molecules (including elements of C, H, O, N, S, and Cl) and experimental data of the isotropic polarizability [90]. Since this subset of the BS dataset has no overlap with QM7b used for training PiNet-χ models, it provides a glimpse of the model performance in real-application scenario. The results of this comparison for EEM, Local, EtaInv and ACKS2 models are shown in figure S2 in the ESI. For small molecules with the number of atoms N_a smaller than 7, all PiNet-χ models underestimate the polarizability. This may not come as a surprise, since only 8 molecules in QM7b have N_a smaller than or equal to 6. For large molecules with $N_a > 28$, both EEM and EtaInv types of models overestimate α_{iso} significantly. This is in contrast with the Local-type model, which underestimates α_{iso}. As shown in figure S1, molecules with large prediction errors are mostly the ones which are planar, multiple sulphur containing, and multiple chlorine containing. Nevertheless, the ACKS2-type of model shows a good overall performance with the root mean square relative error (RMSRE) of about 6% (see table S3 in the ESI), which is at the same level as the B3LYP predictions with respect to the experimental reference [91].

Finally, we also checked the relation between the molecular polarizability and the energy gap. Inspired by the Penn model [92], the isotropic polarizability α_{iso} versus $1/E_g^2$ is plotted in figure 3. As shown in figure 3(a), the HOMO–LUMO gap $E_{HOMO-LUMO}$ and α_{iso} in the QM7b dataset are not really correlated. On the other hand, when approximating η with η_e in EEM and ACKS2, and applying equation (10), clear correlations do present. This agrees with the fact that equation (10) is an approximation to the fundamental gap E_g rather than to the HOMO–LUMO gap. Indeed, in the case of EtaInv-type model, the direct application of equation (10) predicts a much larger E_g as compared to the $E_{HOMO-LUMO}$ labels in the QM7b dataset.

5.2. Size scaling of molecular polarizability

A well-known issue of traditional EEM and QEq types of models is the superlinear scaling of polarizability [52]. This limitation is related to the difficulty of finding a satisfactory semi-local approximation to $\boldsymbol{\eta}$. Thus,

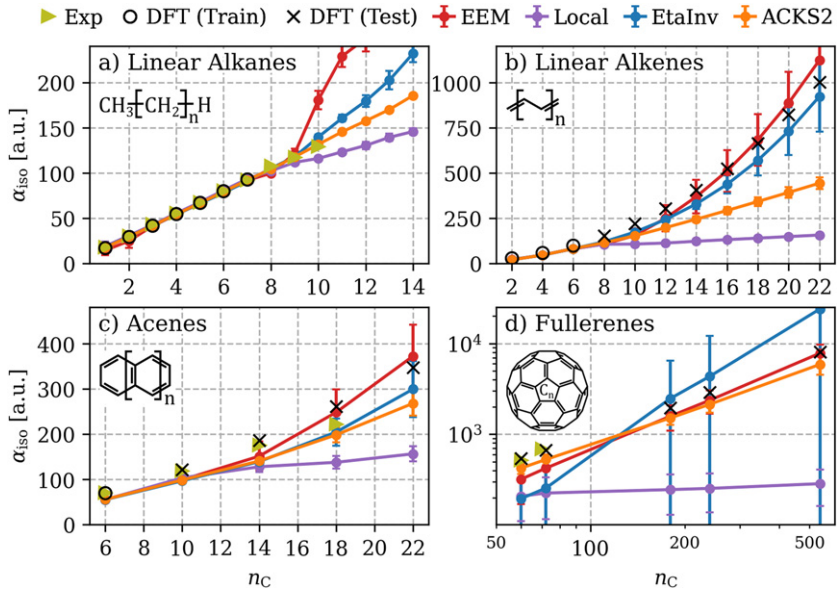

Figure 4. Scaling of the isotropic polarizability α_{iso} predicted from PiNet-χ models with respect to number of carbons n_C in different hydrocarbon series: (a) linear alkanes; (b) linear alkenes; (c) acenes; and (d) fullerenes. Experimental values are taken from reference [93]. DFT labels at B3LYP level of theory are taken from reference [37] for alkane, alkene and acene molecules, and from reference [94] for fullerenes. Test molecules geometries are generated with the RDKit library [95] for linear alkanes, and taken from the QM7b dataset for linear alkenes and acenes, and from Yoshida's fullerene structure library for fullerenes [96].

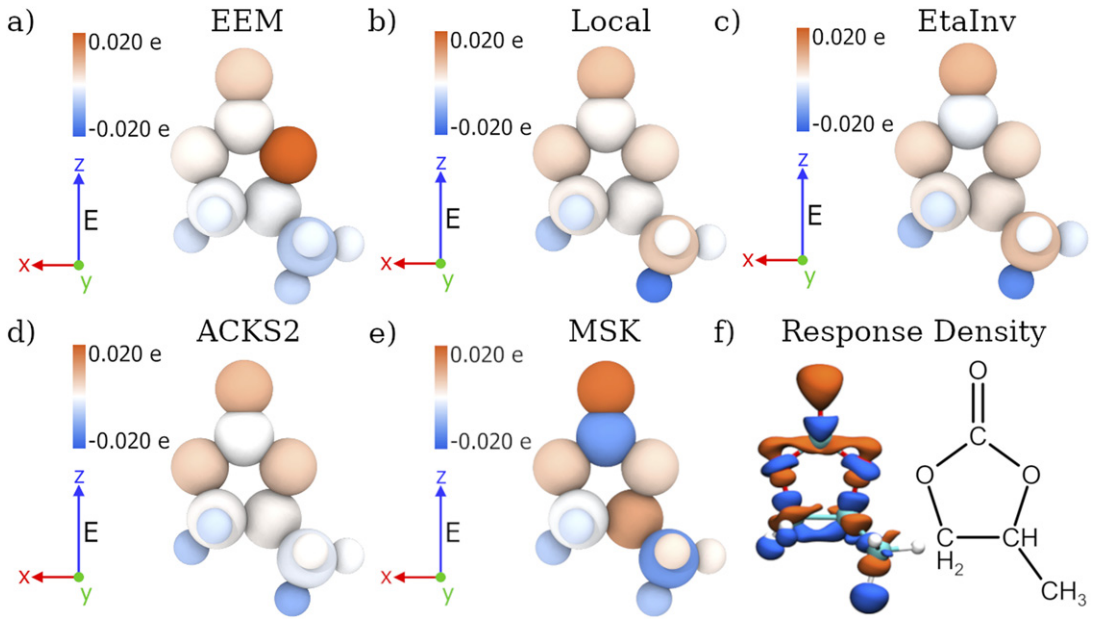

Figure 5. The response charge in propylene carbonate induced by an electric field in the z direction of 0.002 a.u., as predicted by different PiNet-χ models: (a) EEM; (b) Local; (c) EtaInv; (d) ACKS2. The response charge calculated the from MSK scheme and the corresponding DFT response density are shown in (e) and (f). The isosurfaces shown in (h) are $\Delta\rho = -250 \times 10^{-6}$ a.u. (orange) and $\Delta\rho = 250 \times 10^{-6}$ a.u. (blue) respectively.

it is of great interest to see how PiNet-χ models perform in this long-standing challenge, when the kernel is machine-learnt rather than handcrafted. For this purpose, we have taken linear alkanes, linear alkenes, acenes and fullerenes as four examples. Results are shown in figure 4, where a number of interesting observations can be made.

For structures already contained in the training set (open circle in the figure 4), the differences in performance among different models are negligibly small. The EEM-type model, which is usually thought to be incapable of producing the linear scaling of polarizability for linear alkanes, can perform equally well within the training set for $n_c < 7$ and even extrapolate to $n_c = 9$ (figure 4(a)).

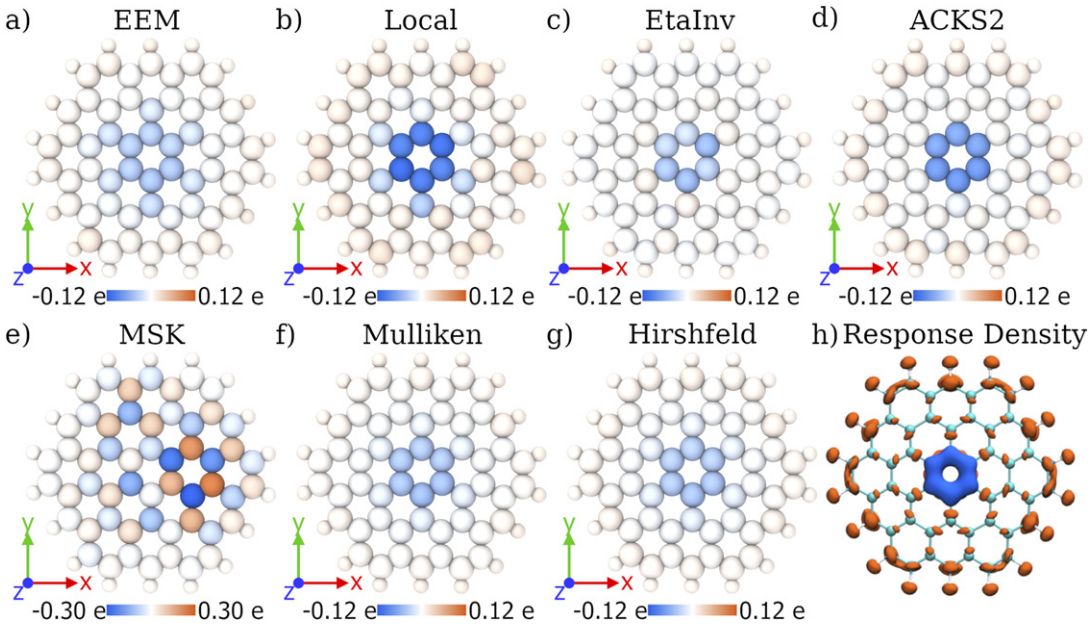

Figure 6. The response charge induced in 54C graphene flake due to the influence of a point charge of $+1e$ located at 2.5 Å above the basal plane, as predicted by different PiNet-χ models: (a) EEM; (b) Local; (c) EtaInv; (d) ACKS2. Response charge calculated using the MSK method, the Mulliken and the Hirshfeld population analyses, and the DFT response-charge density are shown in (e) to (h). The isosurfaces shown in (h) are $\Delta\rho = -500 \times 10^{-6}$ a.u. (orange) and $\Delta\rho = 2500 \times 10^{-6}$ a.u. (blue) respectively.

For structures outside the training set, the situation is divided. Because of its conductor-like behaviour, EEM-type performs very well for conjugated systems (linear alkenes, acenes, fullerenes) but badly for long-chain linear alkanes. On the other hand, ACKS2-type model shows the persistent linear scaling of polarizability for alkane systems but performs less well in conjugated systems apart from the case of fullerenes. EtaInv-type model demonstrates a mixture behaviours between EEM and ACKS2 in general, however, a large variance in the prediction is seen for fullerenes. These observations are also consistent with the prediction results for large molecules in the BS dataset, as stated in the previous section.

In all these models (EEM-type, EtaInv-type and ACKS2-type) mentioned above, the long-range interactions are included in one way or another. In the case of EEM- and ACKS2-type of models, the long-range electrostatics is included in the construction of $\boldsymbol{\eta}_{\mathrm{e}}$ (equation (42)). For the EtaInv-type model, the softness kernel $\boldsymbol{\eta}^{-1}$ was constructed using the local descriptor, but the resulting $\boldsymbol{\chi}$ through equation (9) leads the correct superlinear scaling for conjugated systems. This agrees with a recent finding showing that it is $\boldsymbol{\eta}^{-1}$ rather than $\boldsymbol{\chi}$ that follows the nearsightedness principle of Kohn [97]. In contrast, the local-type model, which postulates $\boldsymbol{\chi}$ as a summation of atomic $\boldsymbol{\chi}_i$ (equation (43)), can only scale linearly with the number of carbon atoms for long-chain molecules. Nevertheless, it is worth noting that the ACKS2-type model, which combines the local description through $\boldsymbol{\chi}_{\mathrm{s}}$ and the non-local description through $\boldsymbol{\eta}_{\mathrm{e}}$, is capable for describing both non-conjugate and conjugate systems as shown here.

5.3. Examples of response charge

As illustrated in figure 1, $\boldsymbol{\chi}$ is not only connected to the polarizability but also linked to the response charge. Here we take two examples to demonstrate, which are not included in the QM7 dataset used to train the models.

In figure 5, the response charges at field strength 0.002 a.u. for propylene carbonate, predicted by different PiNet-χ models, are compared to the corresponding DFT response-charge density. Moreover, we also compare our results to the one calculated using the MSK method, because the electrostatic potential based atomic charge is a popular choice in constructing classical force field of organic molecules [98] and the MSK response charge reproduces reasonably well the induced dipole (therefore the polarizability), as shown in figure S3 in the ESI.

Response charges predicted from Local, EtaInv and ACKS2 types of models look quite similar to each other, in contrast to that predicted using the EEM-type model. Nevertheless, all these models predict that the bottom hydrogen atom of the methyl group has a negative response charge. This is in agreement with what the DFT response-charge density shows.

When comparing response charges predicted from PiNet-χ models to that calculated using the MSK scheme, the carbon atoms in the carbonyl group carries a stronger negative response charge in the MSK scheme than those in PiNet-χ models. This may be due to the fact that response charge in PiNet-χ is described by the s-type basis only. A similar situation happens to the cyano group in the acetonitrile (see figure S4 in the ESI).

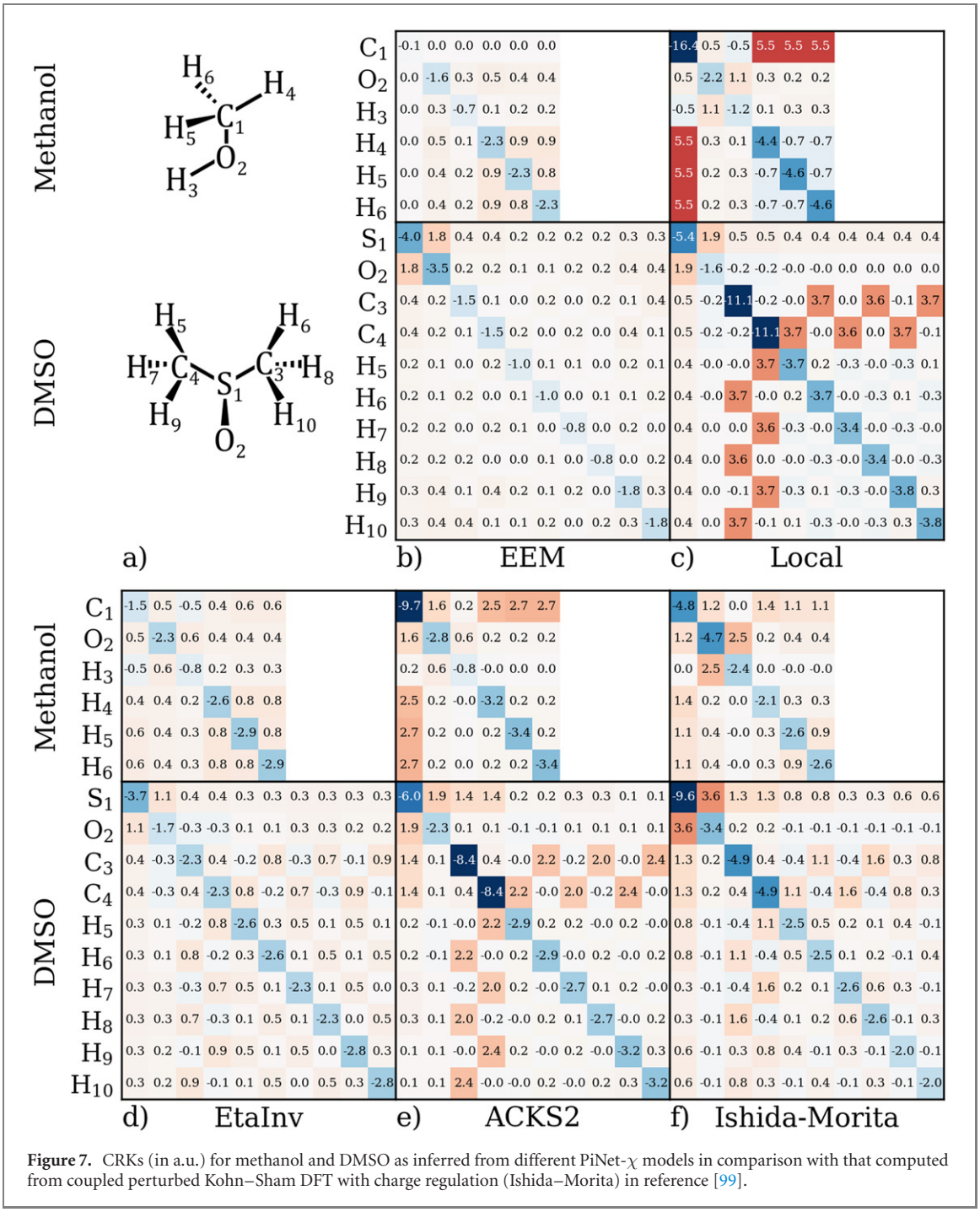

Figure 7. CRKs (in a.u.) for methanol and DMSO as inferred from different PiNet-χ models in comparison with that computed from coupled perturbed Kohn–Sham DFT with charge regulation (Ishida–Morita) in reference [99].

In the meanwhile, we also notice that the carbon connected to the methyl group bears a more positive response charge in the MSK scheme than those in PiNet-χ models. However, inspecting the DFT response-charge density (figure 5), the predictions made by PiNet-χ model look closer to the reference.

Given that the PiNet-χ models can demonstrate a physical scaling behaviour for conjugated hydrocarbons and fullerene as seen in figure 4, and our aim is to model the electrode–electrolyte interface under external bias, it would be of interest to see how well the PiNet-χ models can do for graphene-like systems. Therefore, the second example we show here is the response charge of a graphene flake in response to a point charge of $+1e$. As seen in figure 6, the predicted response charge seems more localized in the Local-type and the ACKS2-type models, in comparison to those predicted from EEM and EtaInv types of models. This is in accord with the scaling plot for linear alkenes and acenes showed in figure 4. Similar results are found in the Mulliken and Hirshfeld population analyses of the response charge, which also agree with the response-charge density from DFT. The only exception is found to be the response charge calculated from the MSK method, where the delocalized nature of the electron density in this case seems to confuse the method.

5.4. Examples of charge response kernel

As PiNet-χ models show the capability for predicting molecular polarizability tensor $\boldsymbol{\alpha}$ and response charge $\mathbf{c}$, one would be curious to know how physical the inferred $\boldsymbol{\chi}$ matrix from ML would be. Indeed, atom-condensed CRKs have been reported in literature for showcase molecules via different means, such as coupled perturbed Kohn–Sham DFT with charge regulation [99] and the Becke population with external perturbation [75]. By comparing to these reference cases, this provides us a way to see what PiNet-χ really 'learned'.

Examples of inferred CRKs by PiNet-χ models for methanol and dimethyl sulfoxide (DMSO) molecules are shown in figure 7, in comparison with those obtained by Ishida and Morita [99]. In the case of methanol, Local, EtaInv and ACKS2 types of models successfully capture the feature of the sub-matrix for the hydroxyl group as well as the positive matrix elements for C–H bonds. Nevertheless, the actual values in the Local-type model are much larger. This is also reflected by a larger induced dipole and polarizability predicted by the Local-type model, as compared to EtaInv and ACKS2 types of models (see figures S3 and S5 in the ESI). In the case of EEM, the matrix element in the corresponding CRK is much smaller, which leads to smaller induced dipole and polarizability shown in figures S3 and S5 in the ESI. For DMSO, despite that the sulfinyl group was not included in the QM7b dataset used to train Pinet-χ models, the inferred CRKs for this extrapolation case by EtaInv and ACKS2 types of models resemble closely that obtained by Ishida and Morita. Nevertheless, the resulting induced dipole and polarizability of DMSO is less well reproduced by PiNet-χ models, especially for the Local-type model (see figures S3 and S5 in the ESI).

In addition, we have also compared examples of CRKs for six smaller molecules, such as CO and H_2O. It is worth noting that these smaller molecules are not included in QM7b dataset and QM7b dataset contains only 8 molecules with the number of atoms smaller than or equal to 6. As shown in figure S6 in the ESI, EEM performs poorly for inferring the physical pattern of CRKs, and erroneous cases, e.g. NH_3 are also found for Local and EtaInv types of models. However, CRKs obtained by ACKS2-type model show a robust feature for all six small molecules, compared to those calculated by Sablon *et al* [75].

6. Conclusion and outlook

In this work, we have bridged atomistic ML and conceptual DFT in order to predict response properties such as molecular polarizability and response charge. This is achieved by providing a unified view of CPE and ACKS2 methods in terms of the CRK, and by exploring the GCNN architecture PiNet.

We show that by introducing environment-dependent parameters in the EEM approximation of the hardness $\boldsymbol{\eta}$, the superlinear scaling of molecular polarizability in linear alkanes, that plagues the EEM type of models, can be remedied in a data-driven fashion. Nevertheless, the extrapolation outside the training set in the EEM-type model is still rather limited. On the other hand, the ACKS2-type model shows a physical scaling and a good out-of-distribution extrapolation of molecular polarizability for both linear alkanes and conjugated systems. The corresponding response charges and CRKs are also consistent with the reference calculations and the literature examples.

One advantage of the CRK formalism for describing response properties lies in the fact that the CRK is translationally, permutationally and rotationally invariant. This makes it a suitable object for applying (scalar) local descriptors. However, as shown in this work, the Local-type model, which decomposes the atom-condensed CRK as a sum of atomic contributions, fails to scale properly with the system size for the conjugated systems. On the other hand, the nearsightedness principle can be explored to describe the softness kernel in the EtaInv-type model and $\boldsymbol{\chi}_s$ in the ACKS2-type model.

The other advantage of the CRK formalism is that it provides the link between the molecular polarizability and the response charge, therefore, the coupling of external field and potential can be introduced naturally. Direct construction of $\boldsymbol{\chi}$ can be performed without matrix inversion in the EtaInv-type model and other model formulations (for example the ACKS2-type model with $\boldsymbol{\eta}_e = 0$, see figures S7 and S8 in the ESI). This means that the CRK-based ML models can be readily and efficiently integrated into the constant potential MD simulations [100] and the fourth-generation high-dimensional neural network potential (4G-HDNNP) [101] for obtaining the response charge.

These advantages of incorporating $\boldsymbol{\chi}$ to describe response properties in ML models can be further explored to handle charge transfer and condensed phase systems. In the original formulation of ACKS2, the application is restricted to the case where the total response charge is zero, i.e. $\mathbf{1}^\top\mathbf{c} = 0$, because of the constraint used to generate the auxiliary Kohn–Sham potential. As showed in the appendix B of this work, this restriction can be lifted by reformulating ACKS2 using Dyson's equation and introducing the dielectric function to the Fukui function. The solution of response charge for the charged system ($\mathbf{1}^\top\mathbf{c} = c_T$) is given in equation (B.13). This extension would allow PiNet-χ models to study charge transfer under external bias, which is important in electrochemical processes. Despite that the examples demonstrated in this work are isolated molecules, the extension of the PiNet-χ framework to periodic systems is straightforward (for example, see figure S9 in the

ESI). For condensed phase systems, the inclusion of dipole–dipole coupling via the dipolar tensor would be necessary [102], and the data-driven approach can be again used to speed up these calculations.

To further improve the model accuracy, the aspects of both descriptor and data should be taken into account. For example, the inclusion of p-type basis functions to expand the response electron density will enable the description of out-of-plane polarizability. Moreover, one could attempt to train CRKs using the response charge, the fundamental band gap E_g or directly the physics-derived CRK, in addition to the molecular polarizability. Apart from that, extending the finite-field based DFTMD for treating metallic electrode and obtaining new (also larger) datasets beyond QM7 used here would provide the necessary labels to generalize PiNet-χ models to other types of materials.

Overall, the reformulation of ACKS2 using the CRK and the development of PiNet-χ framework open up a viable route for introducing finite-field coupling in atomistic simulation of electrochemical systems with ML models. We expect more follow-ups to come out in the near future.

Acknowledgments

This project has received funding from the European Research Council (ERC) under the European Union's Horizon 2020 Research and Innovation Programme (Grant Agreement No. 949012). LK is partly supported by a PhD studentship from the Centre for Interdisciplinary Mathematics (CIM) at Uppsala University. CZ acknowledges the funding through the AI4Research programme at Uppsala University. The calculations were performed on the resources provided by the Swedish National Infrastructure for Computing (SNIC) at C3SE. We thank T Dufils for proof-reading the manuscript.

Data availability statement

All data that support the findings of this study are included within the article (and any supplementary files).

Appendix A. χ in the ACKS2 formalism

The ACKS2 system of equations can be expressed as:

$$\eta_e \mathbf{c} - 1\mu - \boldsymbol{\varphi} = -\Delta\boldsymbol{\nu} \tag{A.1}$$

$$1^\top \mathbf{c} = 0 \tag{A.2}$$

$$\boldsymbol{\chi}_s \boldsymbol{\varphi} - \mathbf{c} - 1\lambda_u = 0 \tag{A.3}$$

$$1^\top \boldsymbol{\varphi} = 0 \quad . \tag{A.4}$$

From equations (A.2) and (A.3) we have

$$1^\top \boldsymbol{\chi}_s \boldsymbol{\varphi} - 1^\top 1\lambda_u = 1^\top \mathbf{c} = 0. \tag{A.5}$$

Since $\mathbf{1}^\top \boldsymbol{\chi}_s = 0$, λ_u must be zero. This means equation (A.3) becomes

$$\mathbf{c} = \boldsymbol{\chi}_s \boldsymbol{\varphi}. \tag{A.6}$$

Multiplying equation (A.1) by $\boldsymbol{\chi}_s$ gives

$$\boldsymbol{\chi}_s \eta_e \mathbf{c} - \boldsymbol{\chi}_s \boldsymbol{\varphi} = -\boldsymbol{\chi}_s \Delta\boldsymbol{\nu}. \tag{A.7}$$

Now we can insert equation (A.6) into the equation above and solve for $\mathbf{c}$. This leads to the following set of equations:

$$\boldsymbol{\chi}_s \eta_e \mathbf{c} - \mathbf{c} = (\boldsymbol{\chi}_s \eta_e - \mathbf{I})\mathbf{c} = -\boldsymbol{\chi}_s \Delta\boldsymbol{\nu} \tag{A.8}$$

$$\mathbf{c} = (\mathbf{I} - \boldsymbol{\chi}_s \eta_e)^{-1} \boldsymbol{\chi}_s \Delta\boldsymbol{\nu} \tag{A.9}$$

$$\mathbf{c} = \boldsymbol{\epsilon}^{-\top} \boldsymbol{\chi}_s \Delta\boldsymbol{\nu}. \tag{A.10}$$

Applying the push-through identity to equation (A.9) and combining it with equation (27), one gets $\boldsymbol{\chi} = \boldsymbol{\chi}_s(\mathbf{I} - \boldsymbol{\eta}_e\boldsymbol{\chi}_s)^{-1}$. Thus, we recover Dyson's equation, i.e. equation (19), if $\boldsymbol{\eta}_e$ is taken as $\mathbf{V}$ and $\boldsymbol{\chi}_s$ is taken as $\boldsymbol{\chi}_0$.

Combining equations (A.6), (A.10) and (A.1), we get

$$\boldsymbol{\varphi} = \boldsymbol{\epsilon}^{-1}\Delta\boldsymbol{\nu} - 1\mu. \tag{A.11}$$

Comparing this to equation (12), one notices that $\boldsymbol{\varphi}$ in ACKS2 is indeed the auxiliary Kohn–Sham potential rather than the Kohn–Sham potential ν_{KS} itself.

Appendix B. Extension to the charged system

Given the Berkowitz–Parr expression of $\boldsymbol{\chi}$ in terms of $\boldsymbol{\eta}^{-1}$ (equation (9)), Dyson's equation of $\boldsymbol{\chi}$ in terms of $\boldsymbol{\chi}_0$ and $\mathbf{V}$ (equation (19)), and the mapping $\boldsymbol{\chi}_s \leftrightarrow \boldsymbol{\chi}_0$ and $\boldsymbol{\eta}_e \leftrightarrow \mathbf{V}$ found here, it would be desirable to establish the connection between $\boldsymbol{\chi}_s$, $\boldsymbol{\eta}_e$ and $\boldsymbol{\eta}$. The procedure to achieve that is to look into the systems where the total response charge is no longer zero.

We start by using the set of ACKS2 equations naively to a perturbation of the total charge system, i.e. replacing equation (A.2) with:

$$1^\top\mathbf{c} = c_T. \tag{B.1}$$

Following the same procedure in appendix A, we have:

$$\lambda_u = -\frac{c_T}{1^\top 1} \tag{B.2}$$

$$\mathbf{c} = \boldsymbol{\chi}\Delta\boldsymbol{\nu} + c_T\frac{\boldsymbol{\epsilon}^{-\top}1}{1^\top 1}. \tag{B.3}$$

Similarly, we can apply the condition equation (B.1) to the CPE equation (39). This leads to the following solution:

$$\mathbf{c} = \boldsymbol{\chi}\Delta\boldsymbol{\nu} + c_T\frac{\boldsymbol{\eta}^{-1}1}{1^\top\boldsymbol{\eta}^{-1}1}. \tag{B.4}$$

Comparing equations (B.3) and (B.4), one may attempt to equate the second term of the first equation with that of the second equation. However, this is unjustified. The second term of equation (B.3) reflects the constraint on the auxiliary Kohn–Sham potential from equation (A.4), which is a convenient choice in ACKS2 rather than a universal solution.

In order to extend ACKS2 to the charged systems, we borrow the idea from the solid-state physics community, which is to introduce the screening through the dielectric function.

Recall that CRK for the interacting system and the non-interacting system are:

$$\chi(\mathbf{r},\mathbf{r}') = \left[\frac{\delta\rho(\mathbf{r})}{\delta\nu(\mathbf{r}')}\right]_{N_0} \tag{B.5}$$

$$\chi_s(\mathbf{r},\mathbf{r}') = \left[\frac{\delta\rho(\mathbf{r})}{\delta\nu_{KS}(\mathbf{r}')}\right]_{N_0}. \tag{B.6}$$

Accordingly, one could define the Fukui function for the interacting system and the non-interacting system as:

$$f(\mathbf{r}) = \left[\frac{\delta\mu}{\delta\nu(\mathbf{r})}\right]_{N_0} \tag{B.7}$$

$$f_s(\mathbf{r}) = \left[\frac{\delta\mu}{\delta\nu_{KS}(\mathbf{r})}\right]_{N_0}. \tag{B.8}$$

Equations (B.5) and (B.6) are connected by equation (16). Taking the transpose of equation (16), one gets:

$$\boldsymbol{\chi} = \boldsymbol{\epsilon}^{-\top}\boldsymbol{\chi}_s. \tag{B.9}$$

This means that $f(\mathbf{r})$ and $f_s(\mathbf{r})$ is related through the dielectric function as well:

$$\mathbf{f} = \boldsymbol{\epsilon}^{-\top}\mathbf{f}_s. \tag{B.10}$$

It is know that the Fukui function can be expressed in terms of the hardness kernel in the following manner [65]:

$$\mathbf{f} = \frac{\boldsymbol{\eta}^{-1}1}{1^{\top}\boldsymbol{\eta}^{-1}1}. \tag{B.11}$$

Combining equations (B.10) and (B.11), one obtains the following expression:

$$\frac{\boldsymbol{\eta}^{-1}1}{1^{\top}\boldsymbol{\eta}^{-1}1} = \frac{\boldsymbol{\epsilon}^{-\top}\boldsymbol{\eta}_{\mathrm{s}}^{-1}1}{1^{\top}\boldsymbol{\eta}_{\mathrm{s}}^{-1}1}. \tag{B.12}$$

Substituting the above relation into equation (B.4) means that the solution for the response charge in the charged systems in terms of χ_{s} and η_{e} should be:

$$\mathbf{c} = \boldsymbol{\chi}\Delta\boldsymbol{\nu} + c_{\mathrm{T}}\frac{\boldsymbol{\epsilon}^{-\top}\boldsymbol{\eta}_{\mathrm{s}}^{-1}1}{1^{\top}\boldsymbol{\eta}_{\mathrm{s}}^{-1}1}, \tag{B.13}$$

where $\boldsymbol{\epsilon}$ depends only on $\boldsymbol{\chi}_{\mathrm{s}}$ and $\boldsymbol{\eta}_{\mathrm{e}}$, and the $\boldsymbol{\eta}_{\mathrm{s}}$ and $\boldsymbol{\chi}_{\mathrm{s}}$ are connected via:

$$\boldsymbol{\chi}_{\mathrm{s}} = -\boldsymbol{\eta}_{\mathrm{s}}^{-1} + \frac{\boldsymbol{\eta}_{\mathrm{s}}^{-1}1 \otimes 1^{\top}\boldsymbol{\eta}_{\mathrm{s}}^{-1}}{1^{\top}\boldsymbol{\eta}_{\mathrm{s}}^{-1}1} \tag{B.14}$$

which is a reminiscent of equation (9).

Finally, it is worthwhile to note that

$$\boldsymbol{\eta} = \boldsymbol{\eta}_{\mathrm{e}} + \boldsymbol{\eta}_{\mathrm{s}} \tag{B.15}$$

with $\boldsymbol{\eta}_{\mathrm{s}}$ defined as:

$$\eta_{\mathrm{s}}(\mathbf{r}, \mathbf{r}') = \frac{\delta^2 T_{\mathrm{s}}}{\delta\rho(\mathbf{r})\delta\rho(\mathbf{r}')}. \tag{B.16}$$

The above equation is a natural consequence by viewing the Kohn–Sham potential ν_{KS} in the non-interacting system as the external potential, which should be taken out when defining the hardness kernel.

ORCID iDs

Chao Zhang https://orcid.org/0000-0002-7167-0840

References

[1] Schmickler W and Santos E 2010 *Interfacial Electrochemistry* (Heidelberg: Springer)
[2] Maier J 2005 *Nat. Mater.* **4** 805–15
[3] Markovic N M 2013 *Nat. Mater.* **12** 101–2
[4] Car R and Parrinello M 1985 *Phys. Rev. Lett.* **55** 2471–4
[5] Marx D and Hutter J 2009 *Ab initio Molecular Dynamics: Basic Theory and Advanced Methods* (Cambridge: Cambridge University Press)
[6] Pham T A, Ping Y and Galli G 2017 *Nat. Mater.* **16** 401–8
[7] Surendralal S, Todorova M, Finnis M W and Neugebauer J 2018 *Phys. Rev. Lett.* **120** 246801
[8] Groß A and Sakong S 2018 *Curr. Opin. Electrochem.* **14** 1–6
[9] Zhang C, Sayer T, Hutter J and Sprik M 2020 *J. Phys.: Energy* **2** 032005
[10] Bouzid A and Pasquarello A 2021 *Atomic-Scale Modelling of Electrochemical Interfaces through Constant Fermi Level Molecular Dynamics* (New York: Wiley) ch 7 pp 221–40
[11] Yang X H, Zhuang Y B, Zhu J X, Le J B and Cheng J 2021 *Wiley Interdiscip. Rev.: Comput. Mol. Sci.* **12** e1559
[12] Nishihara S and Otani M 2017 *Phys. Rev.* B **96** 115429
[13] Hörmann N G, Andreussi O and Marzari N 2019 *J. Chem. Phys.* **150** 041730
[14] Melander M M, Kuisma M J, Christensen T E K and Honkala K 2019 *J. Chem. Phys.* **150** 041706
[15] Schwarz K and Sundararaman R 2020 *Surf. Sci. Rep.* **75** 100492
[16] Bhandari A, Peng C, Dziedzic J, Anton L, Owen J R, Kramer D and Skylaris C K 2021 *J. Chem. Phys.* **155** 024114
[17] Behler J 2021 *Chem. Rev.* **121** 10037–72
[18] Watanabe S, Li W, Jeong W, Lee D, Shimizu K, Mimanitani E, Ando Y and Han S 2020 *J. Phys.: Energy* **3** 012003
[19] Deringer V L, Bartók A P, Bernstein N, Wilkins D M, Ceriotti M and Csányi G 2021 *Chem. Rev.* **121** 10073–141
[20] Unke O T, Chmiela S, Sauceda H E, Gastegger M, Poltavsky I, Schütt K T, Tkatchenko A and Müller K R 2021 *Chem. Rev.* **121** 10142–86
[21] Jia W, Wang H, Chen M, Lu D, Lin L, Car R, Weinan E and Zhang L 2020 Pushing the limit of molecular dynamics with *ab initio* accuracy to 100 million atoms with machine learning *SC20: Int. Conf. for High Performance Computing, Networking, Storage and Analysis* pp 1–14
[22] Deringer V L and Csányi G 2017 *Phys. Rev.* B **95** 094203
[23] Rowe P, Deringer V L, Gasparotto P, Csányi G and Michaelides A 2020 *J. Chem. Phys.* **153** 034702
[24] Hellström M and Behler J 2016 *J. Phys. Chem. Lett.* **7** 3302–6
[25] Shao Y, Hellström M, Yllö A, Mindemark J, Hermansson K, Behler J and Zhang C 2020 *Phys. Chem. Chem. Phys.* **22** 10426–30
[26] Quaranta V, Hellström M and Behler J 2017 *J. Phys. Chem. Lett.* **8** 1476–83
[27] Calegari Andrade M F, Ko H P, Zhang L, Car R and Selloni A 2020 *Chem. Sci.* **11** 2335–41

[28] Schran C, Thiemann F L, Rowe P, Müller E A, Marsalek O and Michaelides A 2021 *Proc. Natl Acad. Sci. USA* **118** e2110077118
[29] Shao Y, Knijff L, Dietrich F M, Hermansson K and Zhang C 2021 *Batteries Supercaps* **4** 585–95
[30] Bereau T, Andrienko D and von Lilienfeld O A 2015 *J. Chem. Theory Comput.* **11** 3225–33
[31] Bleiziffer P, Schaller K and Riniker S 2018 *J. Chem. Inf. Model.* **58** 579–90
[32] Nebgen B, Lubbers N, Smith J S, Sifain A E, Lokhov A, Isayev O, Roitberg A E, Barros K and Tretiak S 2018 *J. Chem. Theory Comput.* **14** 4687–98
[33] Unke O T and Meuwly M 2019 *J. Chem. Theory Comput.* **15** 3678–93
[34] Veit M, Wilkins D M, Yang Y, DiStasio Jr R A and Ceriotti M 2020 *J. Chem. Phys.* **153** 024113
[35] Zhang L, Chen M, Wu X, Wang H, Weinan E and Car R 2020 *Phys. Rev.* B **102** 041121
[36] Knijff L and Zhang C 2021 *Mach. Learn.: Sci. Technol.* **2** 03LT03
[37] Wilkins D M, Grisafi A, Yang Y, Lao K U, DiStasio Jr R A and Ceriotti M 2019 *Proc. Natl. Acad. Sci. USA* **116** 3401–6
[38] Sommers G M, Carlegari Andrade M F, Zhang L, Wang H and Car R 2020 *Phys. Chem. Chem. Phys.* **22** 10592–602
[39] Ko T W, Finkler J A, Goedecker S and Behler J 2021 *Nat. Commun.* **12** 398
[40] Xie X, Persson K A and Small D W 2020 *J. Chem. Theory Comput.* **16** 4256–70
[41] Christensen A S, Faber F A and von Lilienfeld O A 2019 *J. Chem. Phys.* **150** 064105
[42] Gastegger M, Schütt K T and Müller K R 2021 *Chem. Sci.* **12** 11473–83
[43] Keith J A, Vassilev-Galindo V, Cheng B, Chmiela S, Gastegger M, Müller K R and Tkatchenko A 2021 *Chem. Rev.* **121** 9816–72
[44] Parr R G, Donnelly R A, Levy M and Palke W E 1978 *J. Chem. Phys.* **68** 3801–7
[45] Parr R G and Yang W 1989 *Density-Functional Theory of Atoms and Molecules* (Oxford: Oxford University Press)
[46] Geerlings P, De Proft F and Langenaeker W 2003 *Chem. Rev.* **103** 1793–874
[47] Geerlings P, Fias S, Boisdenghien Z and De Proft F 2014 *Chem. Soc. Rev.* **43** 4989–5008
[48] Geerlings P *et al* 2020 *Theor. Chem. Acc.* **139** 36
[49] Mortier W J, Van Genechten K and Gasteiger J 1985 *J. Am. Chem. Soc.* **107** 829–35
[50] Mortier W J, Ghosh S K and Shankar S 1986 *J. Am. Chem. Soc.* **108** 4315–20
[51] Rappé A K and Goddard III W A 1991 *J. Phys. Chem.* **95** 3358–63
[52] Warren G L, Davis J E and Patel S 2008 *J. Chem. Phys.* **128** 144110
[53] Chen J and Martínez T J 2007 *Chem. Phys. Lett.* **438** 315–20
[54] Chelli R, Procacci P, Righini R and Califano S 1999 *J. Chem. Phys.* **111** 8569–75
[55] Nistor R A, Polihronov J G, Müser M H and Mosey N J 2006 *J. Chem. Phys.* **125** 094108
[56] Chen J, Hundertmark D and Martínez T J 2008 *J. Chem. Phys.* **129** 214113
[57] Poier P P and Jensen F 2019 *J. Chem. Theory Comput.* **15** 3093–107
[58] York D M and Yang W 1996 *J. Chem. Phys.* **104** 159–72
[59] Verstraelen T, Ayers P W, Van Speybroeck V and Waroquier M 2013 *J. Chem. Phys.* **138** 074108
[60] Schütt K T, Sauceda H E, Kindermans P J, Tkatchenko A and Müller K R 2018 *J. Chem. Phys.* **148** 241722
[61] Chen C, Ye W, Zuo Y, Zheng C and Ong S P 2019 *Chem. Mater.* **31** 3564–72
[62] Shao Y, Hellström M, Mitev P D, Knijff L and Zhang C 2020 *J. Chem. Inf. Model.* **60** 1184–93
[63] Horton G K and Maradudin A A 1974 *Dynamical Properties of Solids* (New York: American Elsevier)
[64] Keldysh L V, Kirzhnitz D A and Maradudin A A 2012 *The Dielectric Function of Condensed Systems* (Amsterdam: Elsevier Science)
[65] Berkowitz M and Parr R G 1988 *J. Chem. Phys.* **88** 2554–7
[66] Morita A and Kato S 1997 *J. Am. Chem. Soc.* **119** 4021–32
[67] Perdew J P, Parr R G, Levy M and Balduz J L 1982 *Phys. Rev. Lett.* **49** 1691–4
[68] Gázquez J L, Franco-Pérez M, Ayers P W and Vela A 2019 *Int. J. Quantum Chem.* **119** e25797
[69] Brédas J L 2014 *Mater. Horiz.* **1** 17–9
[70] Hedin L 1965 *Phys. Rev.* **139** A796–823
[71] Langreth D C and Perdew J P 1977 *Phys. Rev.* B **15** 2884–901
[72] Gázquez J L and Vela A 1988 *Int. J. Quantum Chem.* **34** 71–6
[73] Cioslowski J and Martinov M 1994 *J. Chem. Phys.* **101** 366–70
[74] Chelli R and Procacci P 2002 *J. Chem. Phys.* **117** 9175–89
[75] Sablon N, De Proft F, Ayers P W and Geerlings P 2010 *J. Chem. Theory Comput.* **6** 3671–80
[76] Stone A 1985 *Mol. Phys.* **56** 1065–82
[77] He K, Zhang X, Ren S and Sun J 2016 Deep residual learning for image recognition *Proc. IEEE Conf. on Computer Vision and Pattern Recognition (CVPR)*
[78] Yang Y, Lao K U, Wilkins D M, Grisafi A, Ceriotti M and DiStasio R A 2019 *Sci. Data* **6** 152
[79] Stephens P J, Devlin F J, Chabalowski C F and Frisch M J 1994 *J. Phys. Chem.* **98** 11623–7
[80] Dunning T H Jr 1989 *J. Chem. Phys.* **90** 1007–23
[81] Abadi M *et al* 2016 arXiv:1603.04467
[82] Kingma D P and Ba J 2014 arXiv:1412.6980
[83] Pascanu R, Mikolov T and Bengio Y 2013 On the difficulty of training recurrent neural networks *Proc. 30th Int. Conf. on Machine Learning* vol 28 (PMLR) pp 1310–8
[84] Frisch M J *et al* (2016) *Gaussian 09, Revision A.02* (Wallingford, CT: Gaussian, Inc.)
[85] Singh U C and Kollman P A 1984 *J. Comput. Chem.* **5** 129–45
[86] Besler B H, Merz K M Jr and Kollman P A 1990 *J. Comput. Chem.* **11** 431–9
[87] Mulliken R S 1955 *J. Chem. Phys.* **23** 1833–40
[88] Hirshfeld F L 1977 *Theor. Chim. Acta* **44** 129–38
[89] Hickey A L and Rowley C N 2014 *J. Phys. Chem.* A **118** 3678–87
[90] Bosque R and Sales J 2002 *J. Chem. Inf. Comput. Sci.* **42** 1154–63
[91] Hait D and Head-Gordon M 2018 *Phys. Chem. Chem. Phys.* **20** 19800–10
[92] Penn D R 1962 *Phys. Rev.* **128** 2093–7
[93] Rumble J 2021 *CRC Handbook of Chemistry and Physics: A Ready-Reference Book of Chemical and Physical Data* (Boca Raton, FL: CRC Press)
[94] Brand M, Ahmadzadeh K, Li X, Rinkevicius Z, Saidi W A and Norman P 2021 *J. Chem. Phys.* **154** 074304
[95] Landrum G *et al* (2021) *RDKit: Open-Source Cheminformatics 2021_09_2 (Q3 2021) Release*

[96] Yoshida M 2021 VRML gallery of fullerenes http://jcrystal.com/steffenweber/gallery/Fullerenes/Fullerenes.html (accessed 6 December 2021)
[97] Fias S, Heidar-Zadeh F, Geerlings P and Ayers P W 2017 *Proc. Natl. Acad. Sci. USA* **114** 11633–8
[98] Bayly C I, Cieplak P, Cornell W and Kollman P A 1993 *J. Phys. Chem.* **97** 10269–80
[99] Ishida T and Morita A 2006 *J. Chem. Phys.* **125** 074112
[100] Scalfi L, Salanne M and Rotenberg B 2021 *Annu. Rev. Phys. Chem.* **72** 189–212
[101] Ko T W, Finkler J A, Goedecker S and Behler J 2021 *Acc. Chem. Res.* **54** 808–17
[102] Böttcher C J F 1993 *Theory of Electric Polarization* (Amsterdam: Elsevier)